Lab on a Chip

PAPER

View Article Online
View Journal | View Issue

Check for updates

Cite this: *Lab Chip*, 2025, **25**, 5329

High-throughput multimodal optofluidic biophysical imaging cytometry

Thiel Lee, †[a] Evelyn H. Y. Cheung, †[a] Kelvin C. M. Lee, [ac] Dickson M. D. Siu, [ac] Michelle C. K. Lo, [ac] Edmund Y. Lam, [a] Ruchi Goswami, [b] Salvatore Girardo, [b] Kyoohyun Kim, [b] Felix Reichel, [b] Marketa Kubankova, [b] Martin Kräter, [b] Jochen Guck [b] and Kevin K. Tsia *[ac]

Received 20th April 2025,
Accepted 15th August 2025

DOI: 10.1039/d5lc00381d

rsc.li/loc

Traditional biophysical cytometry has been limited by its low-dimensional phenotyping characteristics, often relying on only one or a few cellular biophysical phenotypes as readouts. This has perpetuated the perception that biophysical cytometry lacks the power to determine cellular heterogeneity. Here, we introduce a multimodal biophysical cytometry platform, termed quantitative phase morpho-rheological (QP-MORE) cytometry, which simultaneously captures a collection of high-resolution biophysical and mechanical phenotypes of single cells at ultrahigh throughput (>10 000 cells per s). Combined with a microfluidic constriction channel design, QP-MORE integrates ultrafast single-cell quantitative phase imaging (QPI) and high-throughput deformability cytometry to resolve subcellular structures and whole-cell rheology in a single pass. QP-MORE's optofluidic design enables label-free, multi-contrast imaging of cells flowing at ~1 m s^{-1}, achieving subcellular resolution unmatched by existing deformability-based platforms. To validate its precision, we developed a robust calibration protocol ensuring high accuracy in morpho-rheological measurements. We also deployed QP-MORE to dissect drug-induced biophysical heterogeneity in HL60 leukemia and MDA-MB-231 breast cancer cells treated with latrunculin B (actin depolymerizer) and cytochalasin D (actin capping agent). QP-MORE not only revealed drug-specific subcellular biophysical signatures, but also achieved 99% accuracy in classifying drug mechanisms, surpassing deformability cytometry (78–94%). This underscores the potential of QP-MORE in expanding the capability of biophysical cytometry, especially in advancing our understanding of cellular heterogeneity and drug interactions.

Introduction

Recent innovations in imaging cytometry, particularly when integrated with microfluidics, have transformed our ability to visualize and analyze cells at single-cell resolution. These innovations not only allow for high-resolution imaging but also enable comprehensive, quantitative analysis of diverse cell morphological traits.[1–3] Apart from the gold standard fluorescence imaging,[4–11] label-free imaging[12–14] has also rapidly evolved, allowing read-out of intrinsic biophysical properties of cells—such as cell deformability, dry-mass-density (DMD) and their subcellular distribution—that provide unprecedented insights into the underlying molecular state of cells and are indicative of various cellular processes.[14] To name a few, *changes in cell size and mass* are closely associated with cell-cycle progression, proliferation, and apoptosis, and their alterations can indicate abnormalities in cell proliferation or cell death pathways;[15,16] *cell stiffness* is linked to cellular behaviours such as metastatic potential and stem cell multipotency;[17–20] *subcellular/nuclear organisation* plays a critical role in gene regulation and cellular function/dysfunction;[21,22] *mechanical changes in the cytoskeleton and nucleus* are major contributors to cellular mechanics.[23] Likewise, alterations in cytoskeletal and nuclear stiffness can serve as surrogate markers for drug responses.[17,24] By harnessing these biophysical properties, researchers can gain insights into cellular behaviour, disease progression, and therapeutic interventions.

Despite these strengths, biophysical cytometry has traditionally been limited in its ability to capture cellular heterogeneity due to constraints in both throughput and the content (*i.e.*, dimensionality) of phenotyping.[25] To overcome these limitations, advanced techniques have been developed

[a] *Department of Electrical & Electronic Engineering, The University of Hong Kong, Pokfulam Road, Hong Kong. E-mail: tsia@hku.hk*
[b] *Max Planck Institute for the Science of Light & Max-Planck-Zentrum für Physik und Medizin, 91058 Erlangen, Germany*
[c] *Advanced Biomedical Instrumentation Centre, Hong Kong Science Park, Shatin, New Territories, Hong Kong*
† Authors have equal contributions.

to increase the measurement throughput and/or information content of the phenotyping readouts. Microelectromechanical systems (MEMS) resonators[26] have been developed to measure cell deformability at a rate of approximately 10 to 100 cells per minute to an hour. This enables the analysis of a larger number of cells, providing a more comprehensive view of cellular heterogeneity. Additionally, approaches such as hydrodynamic stretching[9,27] and inertial-force-based stretching[28,29] have demonstrated the ability to measure cell deformability at a moderate throughput of approximately 100 to 1000 cells per second. A method based on hydrodynamic stretching could achieve an imaging throughput of 2000 cells per s, but could not perform subcellularly resolved biophysical phenotyping.[27] These deformability cytometry (D–C) methods utilise fluidic forces to stretch cells and assess their mechanical properties in different disease conditions, offering valuable insight into cell health and advancing the study of cells, diseases, diagnoses, treatments, medications, *etc.*[9,30–34] However, it can only offer bright-field image contrast with limited details in morphological phenotyping, and its imaging throughput is limited to 1000 cells per second.[31,32,35,36]

A parallel advancement of biophysical cytometry is quantitative phase imaging (QPI).[37–41] QPI generates maps of optical path length delays caused by the cell body, enabling the label-free quantification of subcellular-resolvable biophysical morphology and thus functional assessments of cell types and states.[34,42–45] Specifically, in QPI-based flow cytometry, imaging throughput can be scaled with flow speed. However, increasing the flow speed often results in severe image motion blur and resolution degradation, primarily due to the limitations of current camera technology. Additionally, the reduced sensitivity of cameras at high imaging rates further hampers the throughput of existing QPI flow cytometers, which typically reach up to ~1000 cells per s,[31,36] unless augmented by deep learning approaches.[25,46]

To address the aforementioned challenges, we present a new approach, coined quantitative phase morpho-rheological (QP-MORE) cytometry, offering a new capability of multimodal biophysical imaging cytometry at high throughput. QP-MORE cytometry enables ultrafast single-cell QPI within a microfluidic system designed to manipulate cell deformation. This new technique distinguishes itself in two key ways: first, QP-MORE cytometry supports high-speed single-cell QPI within a custom-designed microfluidic platform, achieving throughputs exceeding 10 000 cells per second—at least 10 to 100 times higher than existing state-of-the-art QPI cytometry and deformability cytometry technologies.[30–32,36] Second, going beyond conventional QPI or deformability cytometry, QP-MORE enables deeper biophysical phenotyping, providing comprehensive readouts related to optical-density, mass-density, and cell deformability, as well as their *interrelationships* (Fig. 1). We demonstrated that QP-MORE cytometry can detect not only bulk biophysical or mechanical changes in drug-treated cells but also subtle alterations in subcellular mass and optical-density distribution. This capability allows for comprehensive, high-dimensional QP-MORE profiling of single cells, offering richer insights into the biophysical properties of cells than previously possible with traditional methodologies.

Results

Quantitative phase morpho-rheological (QP-MORE) cytometry

The QP-MORE cytometry employs the ultrahigh-throughput line-scanning QPI technique named multi-ATOM (multiplexed asymmetric-detection time-stretch optical microscopy)[38,39,41] to read out a multitude of biophysical and mechanical properties of single cells (Fig. 1). The key strength of multi-ATOM is its ultrafast laser-scanning operation (>MHz) that allows subcellular-resolution QPI at ultrahigh microfluidic imaging throughput (>10 000 cells per s).[34,38,42,43] In contrast to the previous work of multi-ATOM and deformability cytometry, the microfluidic chip employed in this work was designed to support not only high-speed precision microfluidic flow but also the deformation of single cells at the same flow speed—>10-times higher than previous deformability cytometry demonstrations.[30–32,36]

The microfluidic chip is designed to force cells to align into a single stream using the sheath flow and the constriction channel (Fig. 1A and S2). Specifically, the channel is designed to have a sharp constriction to confine the cell stream into a compartment (with a cross-sectional size of 20 μm × 20 μm) before they pass through the laser line-scan interrogation point within the constriction section (300 μm in length). The channel constriction introduces a high degree of deformation to individual cells, by inducing hydrodynamic shear stress and pressure gradient in the microfluidic flow.[9,31,32,36] Typically, the cells are deformed into a bullet-like shape with the bullet head pointing forward along the fluid flow.

Multi-ATOM captured the images of individual single cells flowing within the constriction channel through laser line-scan illumination, which is configured with a velocity calibration module for accurate deformability measurement (see next section). Multi-ATOM reconstructs three complementary image contrasts from raw line-scan data: (1) differential phase contrast (DPC),[47] which enhances edges and subcellular textures *via* phase gradient imaging; (2) quantitative phase image (QPI), providing optical path delay maps for DMD quantification (resolution: 0.001 pg fl^{-1}); and (3) local variance of DMD image (LVD), highlighting subcellular spatial heterogeneity (Fig. 1B). From these contrasts, we extract 86 quantitative morpho-rheological features per cell, spanning fine-grained textures (*e.g.*, phase skewness, fit texture variance), coarse-grained biophysical parameters (*e.g.*, cell area, total dry mass), and bulk metrics (*e.g.*, cell size, deformability) (Fig. 1C). This hierarchical profiling strategy (from fine-grained textures to bulk) has been found effective for the interpretation of cell morphology

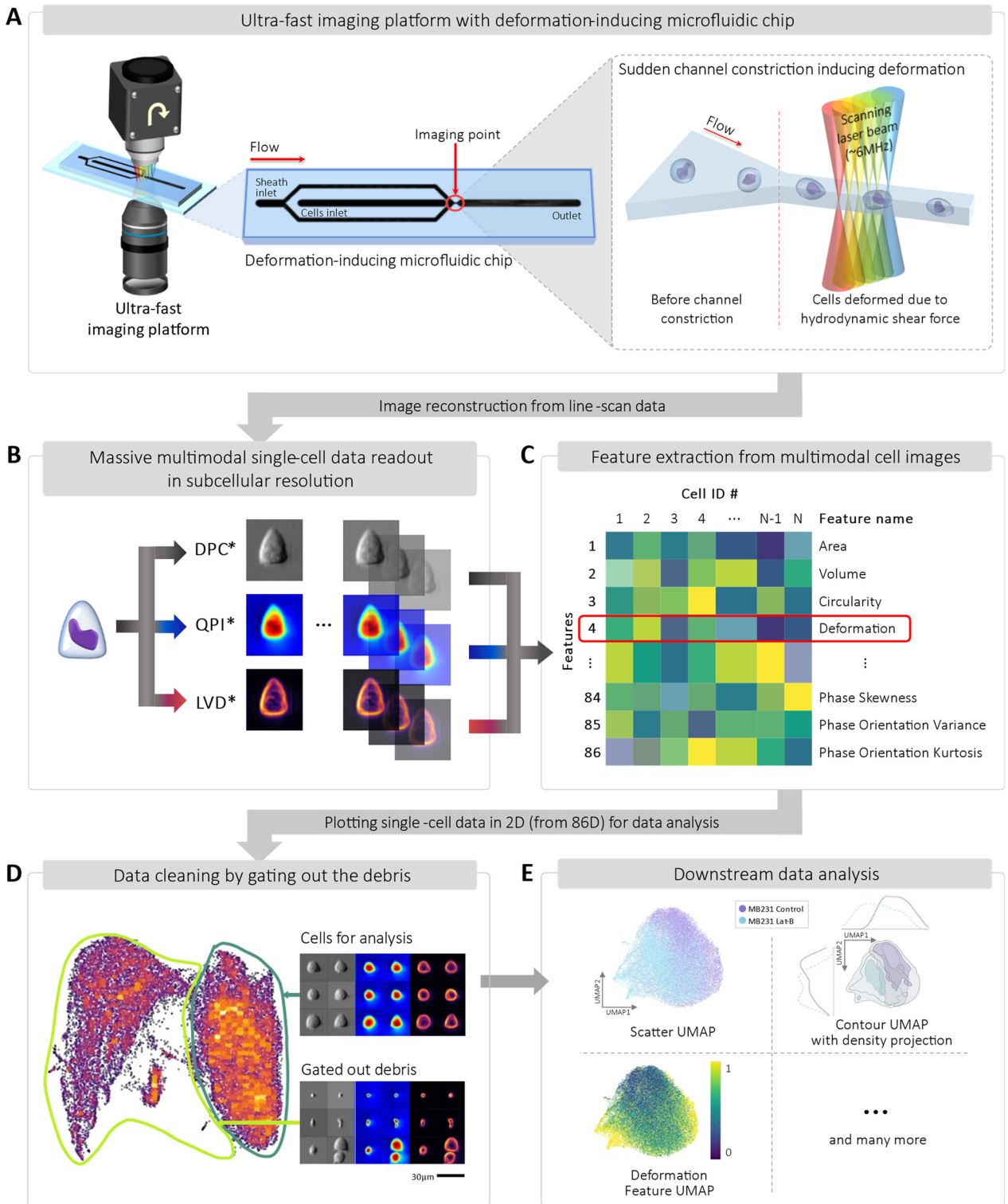

Fig. 1 Workflow of quantitative phase morpho-rheological (QP-MORE) cytometry. (A) Microfluidic chip is designed to force the cells to align into a single stream using the sheath flow in the constriction channel (of width of 20 μm) while also inducing hydrodynamic shear stress, which deforms the cells into a bullet-like shape along the flow direction. The ratio of the flow rate of the sample to the sheath is 1 : 3. The laser line-scan beam interrogates the deformed cell at the imaging point in the constriction channel for capturing the cell images. (B) The consecutive line-scans are then used to reconstruct the multi-contrast images: differential phase contrast (DPC)*, quantitative phase image (QPI)*, and local variance of dry-mass-density (DMD) image (LVD)* at a real-time imaging throughout of up to ~10 000 cells per second. (C) A total of 86 optophysical features (phenotypes) are quantitatively extracted from a single cell following a spatially hierarchical manner. (D) The entire population of cell data are visualized in UMAP and are gated to remove debris data for a more refined downstream analysis. (E) Various different biophysical cytometric analyses can be performed, including clustering plots, contour plots with density projection, and UMAP color-coded with feature expression.

in a more systematic and semantic way.[43] The complete list of 86 features employed in this study can be found in Table S1.

The 86-dimensional QP-MORE single-cell datasets are analyzed and displayed in the uniform manifold approximation and projection (UMAP) plot, based on which preliminary screening/gating of debris (Fig. 1D) and downstream statistical phenotypic analysis can be performed (Fig. 1E).

QP-MORE addresses two critical limitations of prior biophysical cytometers. First, it eliminates the trade-off between throughput and resolution, achieving >10 000 cells per s while resolving subcellular features—surpassing deformability cytometry (1000 cells per s, bright-field-only[31]) and conventional QPI (~1000 cells per s[4,48]). Second, it captures a comprehensive catalogue of biophysical and mechanical properties, integrating QPI-derived mass-density mapping with deformability-based mechanical profiling. While existing systems focus on bulk parameters (*e.g.*, whole-cell stiffness), QP-MORE's multimodal design uniquely enables the exploration of correlative relationships between subcellular features, such as mass distribution and local stiffness heterogeneity. This capability positions QP-MORE as a valuable tool for probing mechanobiological mechanisms in drug response studies and disease models.

Velocity calibration (VC) and validation

The line-scan imaging operation of multi-ATOM captures cell images by sequentially recording 1D laser scans as cells flow through the interrogation point. Unlike 2D full-frame imaging, this approach reconstructs 2D images by stitching successive line scans. Crucially, cells with different sizes traverse the constriction channel at different speeds due to hydrodynamic resistance:[31,49,50] smaller cells experience lower drag and accelerate, while larger cells decelerate. This velocity disparity distorts image reconstruction, elongating smaller cells and compressing larger ones along the flow axis. Furthermore, discrepancies between the syringe pump's nominal flow rate and the actual velocity within the constriction channel—exacerbated by transient pump fluctuations (typically ~1–5% error)—introduce additional uncertainty.

Without accounting for these variations, extracted biophysical features (*e.g.*, cell size, deformability) become

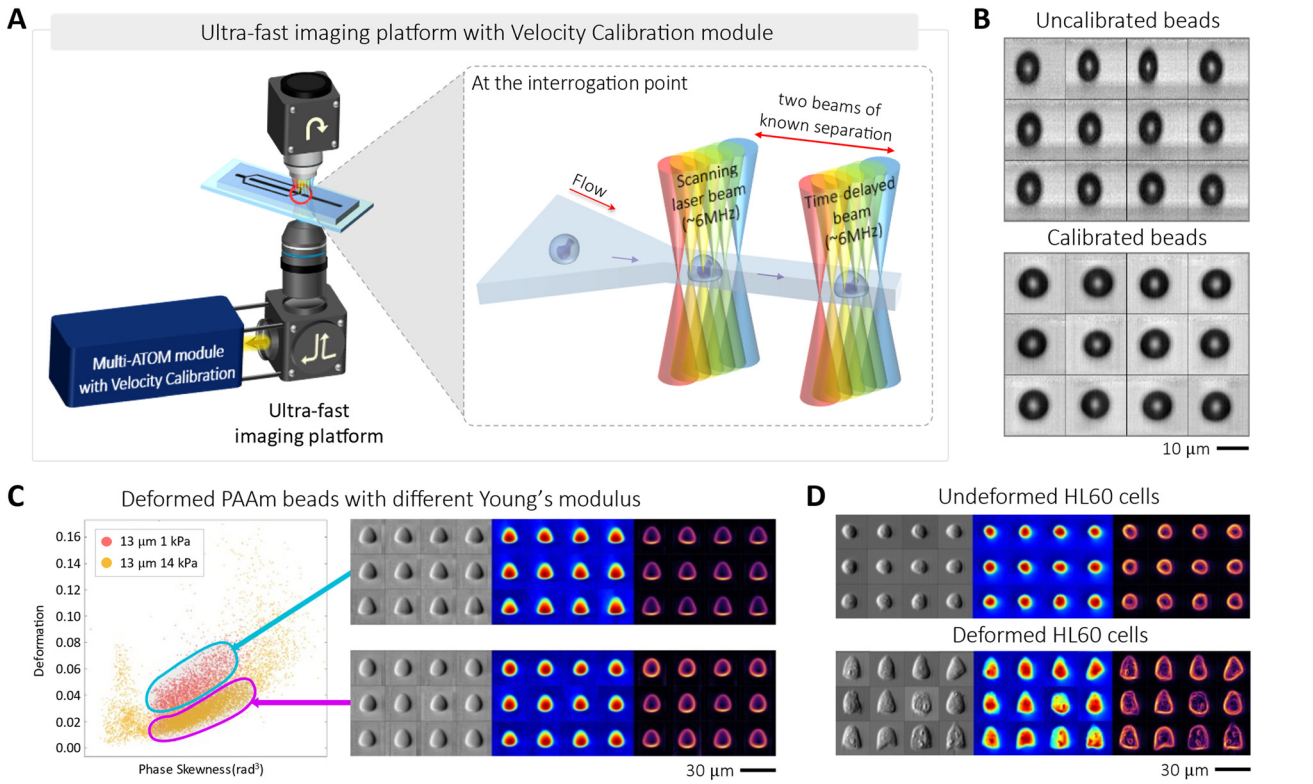

Fig. 2 Ultra-fast imaging platform with velocity calibration module. Schematic of the ultrafast imaging platform with the VC module added to the QP-MORE system. Optical pathways were modified to introduce a time-delayed beam that is identical to the scanning laser beam (line-scan rate was compromised from 10.08 MHz to 6.04 MHz). The difference in the number of line-scans the cell took to pass through both the beams is used to calculate the actual velocity of the cell. (B) VC using 10 μm PMMA beads, showing images of beads before and after calibration. Scale bar = 10 μm. (C) Sample cell images of deformed and undeformed cells constructed after the VC module was installed. Scale bar = 30 μm. (D) Validation of VC using 13 μm PAAm beads of stiffness 1 kPa and 14 kPa each. PAAm beads with lower stiffness is showing a greater degree of deformation as expected.

inherently unreliable, as image-derived metrics scale with flow velocity. For instance, a cell traveling faster than assumed will appear artificially contracted, leading to an underestimation of its true cell size. The velocity variation could also result in distortion of the actual sub-cellular textures and thus confound the overall morphological profiling and analysis. To eliminate these artefacts, the VC module is essential to directly measure the instantaneous velocity of each cell, enabling pixel-to-micron calibration during image reconstruction. By dynamically adjusting for velocity heterogeneity,[51] VC ensures quantitative accuracy in morpho-rheological phenotyping across diverse cell populations (Fig. 2).

We developed a "*dual-laser-beam*" VC module integrated into multi-ATOM's optical path (Fig. 2A). Two time-delayed laser beams, spatially separated by 10 μm, sequentially interrogate each cell. Leveraging the fixed beam separation (D = 10 μm) and the system's laser repetition rate (f_{laser} = 6.04 MHz), the true cell velocity is calculated as

$$v = \frac{D}{N} f_{\text{laser}}$$

where N is the number of line scans between beam crossings that can be monitored in real-time. Thus, this single-cell velocity measurement compensates for size- and pump-induced speed variations, ensuring accurate reconstruction of cell morphology. Note that the 10 μm separation between the two laser beams in the VC module represents an optimal balance between signal fidelity and throughput. A narrower spacing risks optical crosstalk, where overlapping signals from the dual beams distort image reconstruction, while a wider spacing increases the likelihood of signal interference from sequentially passing cells, necessitating slower flow rates to avoid data overlap and compromising throughput. The 10 μm distance minimizes these trade-offs, ensuring robust velocity measurement without sacrificing imaging speed or resolution.

By reconstructing images using the true velocity, QP-MORE eliminates velocity-dependent distortions, as demonstrated by robustly uniform circular profiles of polymethylmethacrylate (PMMA) beads post-VC (Fig. 2B). Uncalibrated beads, in contrast, exhibit variable compression due to uncorrected (and unstable) flow mismatches. The VC module's efficacy was further validated using polyacrylamide (PAAm) microgels of defined stiffness (1 kPa and 14 kPa, mimicking soft and stiff cells, respectively). Post-VC, soft microgels deformed consistently by an average of 0.0648, while stiff microgels showed minimal strain (0.0485 in mean) (Fig. 2C). Similarly, human leukemia (HL60) cells displayed distinct deformation profiles after VC, with undeformed and deformed subpopulations clearly resolved (Fig. 2D). These results confirm that VC not only corrects velocity artifacts but also enhances the precision of biophysical phenotyping—a capability unattainable with conventional deformability cytometry or uncorrected QPI. We note that all the morphological profiling steps and analyses (Table S1) in this work were performed based on the post-VC images.

QP-MORE dissects multiscale biophysical responses to actin-targeted therapy

To demonstrate QP-MORE's ability to resolve drug-induced biophysical remodeling, we analyzed MDA-MB-231 breast cancer cells treated with latrunculin B (Lat-B), a drug that destabilizes actin microfilaments. Actin networks are primary contributors to cellular stiffness at low mechanical strains, and their depolymerization is expected to soften cells while disrupting subcellular mass organization.[52,53] QP-MORE captured these changes hierarchically, from whole-cell mechanics to minute density fluctuations, offering unprecedented insight into the biophysical attributes of cytoskeletal disruption. Note that the interpretations are made and the results are derived in relation to the control sample data.

At the whole-cell level, Lat-B-treated cells show an obvious increase in deformability (mean value 11.6% higher than that of the control sample; Cliff's delta d = 0.15) with minimal cell size changes (d = −0.06) (Fig. 3A), consistent with prior deformability cytometry studies.[32] Interestingly, QP-MORE revealed a further association of this softening with a concurrent 9.92% reduction in DMD (0.0432 pg fl^{-1} *vs.* 0.0393 pg fl^{-1}; d = −0.17), directly implicating actin filament dissolution as the source of both mechanical and compositional changes (Fig. 3B). This inverse deformability–density relationship—previously obscured in single-modality assays—highlights the value of multimodal profiling for mechanistic studies.

Beyond bulk metrics, QP-MORE quantified 86 subcellular features related to the optical density and mass density distributions within the cells. These features are derived from three different image contrasts: bright-field (BF), QPI, and LVD. Note that the multimodal images shown on the figures are in DPC, QPI and LVD, whereas BF, QPI and LVD images were used for quantitative feature extraction. DPC is used for visualization as it displays higher contrast than BF.

UMAP analysis based on these 86 features resolved the drug response into three clusters (Fig. 3C): untreated cells (group I) and Lat-B-treated cells which can be further split into partially disrupted (group II) and severely disrupted (group III) subpopulations, distinguished by progressive mass homogenization and texture fragmentation. Analyzing the "expression" variation of different subcellular biophysical morphological features in UMAP, one can examine how QP-MORE links biophysical changes to Lat-B's mechanism of action (Fig. 3D, E, S4 and S5). For instance:

- DMD centroid displacement measures the deviation between a cell's geometric center and the centroid of its DMD distribution. A decrease in this metric (d = 0.06 in group III) could reflect mass redistribution as actin depolymerizes from organized cortical bundles, homogenizing intracellular mass (Fig. 3D).

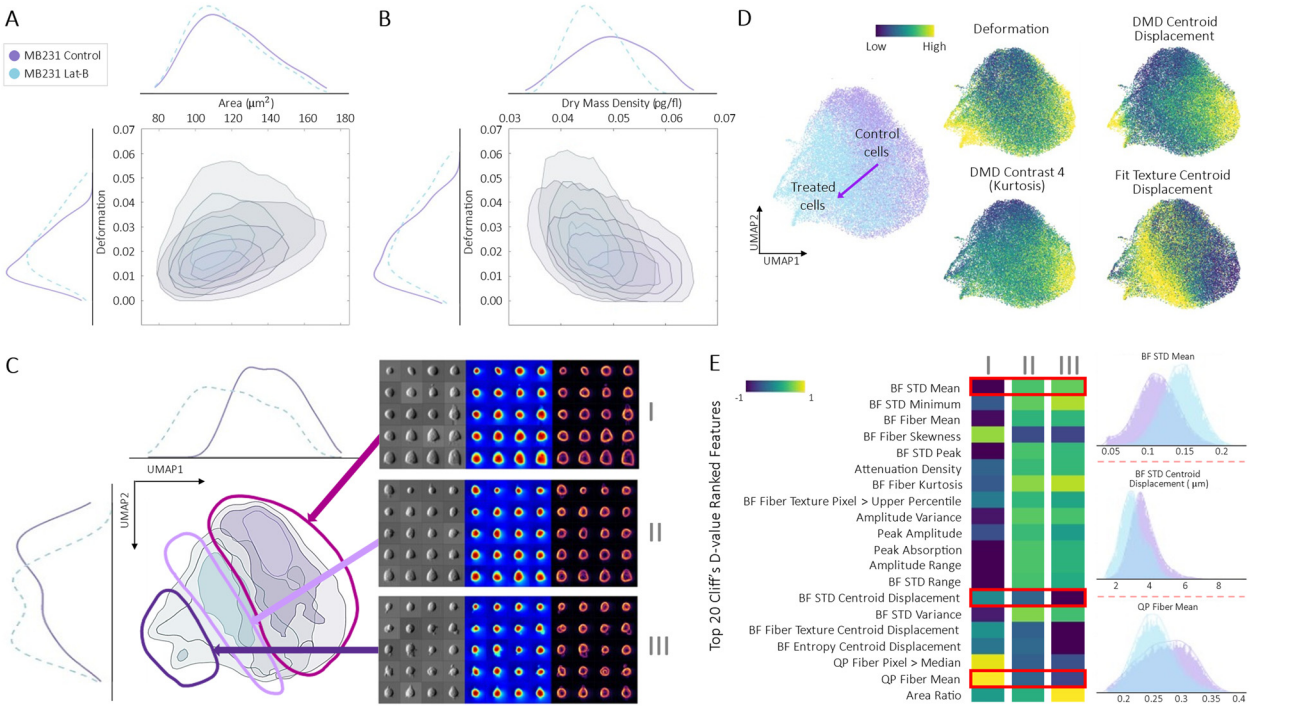

Fig. 3 Analysis of MDA-MB231 control cells (purple) and latrunculin-B treated cells (blue). (A) Contour map of deformation *vs.* area for control and treated cells showing different range of deformation for similar cell area range. (B) Contour map of deformation *vs.* DMD for the same population showing DMD distribution over a range of deformation. (C) UMAP of 86 features extracted from QP-MORE, subdivided into 3 groups for data analysis, according to their density. (D, left) The overall distribution of control and treated population that shows a clear trend, and (right) four selected feature UMAPs showing the feature trend over the whole population. (E, left) List of features ranked in higher Cliff's delta value (*d*-value), color-coded (normalized from −1 to 1) by clusters categorized in accordance with (C). (right) Histogram plots of features highlighted in red from the heatmap. Note the greater degree of overlap as feature ranking increases. BF = bright-field (BF) image-derived features; QP = quantitative phase (QP) image-derived features; STD = standard deviation.

• DMD contrast 4 (kurtosis) quantifies the "peakedness" of DMD distribution. Reduced kurtosis (d = −0.04 in group II and III) indicates flattened mass profiles, consistent with the well-known actin filament breakdown into diffuse G-actin pools (Fig. 3D).

• Fit texture centroid displacement tracks asymmetry in subcellular texture patterns. Its increase (d = 0.15 in group II and III) signals fragmented cytoskeletal remnants—likely detached actin aggregates—displacing texture centers (Fig. 3D).

As a result, these features map directly to Lat-B's mechanism: actin depolymerization dissolves polarized filament networks, dispersing mass (reduced DMD centroid displacement) and flattening density gradients (reduced DMD contrast 4, kurtosis), while residual filament fragments create chaotic texture asymmetries (increased fit texture centroid displacement). Using the top 20 discriminative features ranked by effect size ($0.18 < d < 0.48$), we constructed distinct biophysical profiles for each group, revealing the heterogeneity of Lat-B-induced effect. We observe that the morphological profiles are distinctively different between control (group I) and the Lat-B treated population (group II and III). Critically, QP-MORE detected subtle differences between groups II and III. For instance, group III exhibits higher deformation over group II (0.0307 *vs.* 0.0855) (Fig. 3D), lower fiber-like structure alignment (as reflected in lower BF/QP fiber mean), reduced weighted centroid displacement patterns (as indicated by the lower BF STD/entropy centroid displacement) (Fig. 3E).

This granular biophysical morphological analysis—unachievable with conventional deformability cytometry or QPI—underscores QP-MORE's unique ability to recapitulate cellular responses into mechanistically interpretable biophysical states. By correlating subcellular texture shifts with whole-cell mechanics, the platform offers a valuable tool for drug mechanism studies.

QP-MORE reveals subtle subcellular biophysical changes in different actin-targeting drug treatments

To demonstrate QP-MORE's ability to resolve subtle differences in drug-induced biophysical remodelling, we selected two actin-targeting agents—latrunculin B (Lat-B) and cytochalasin D (Cyto-D)—that perturb cytoskeletal dynamics through distinct yet overlapping mechanisms.[53] Lat-B sequesters actin monomers, blocking polymerization into filaments, while Cyto-D caps the barbed ends of existing filaments, halting elongation and accelerating depolymerization.[52,53] Despite both drugs inducing actin network collapse, their divergent molecular actions produce

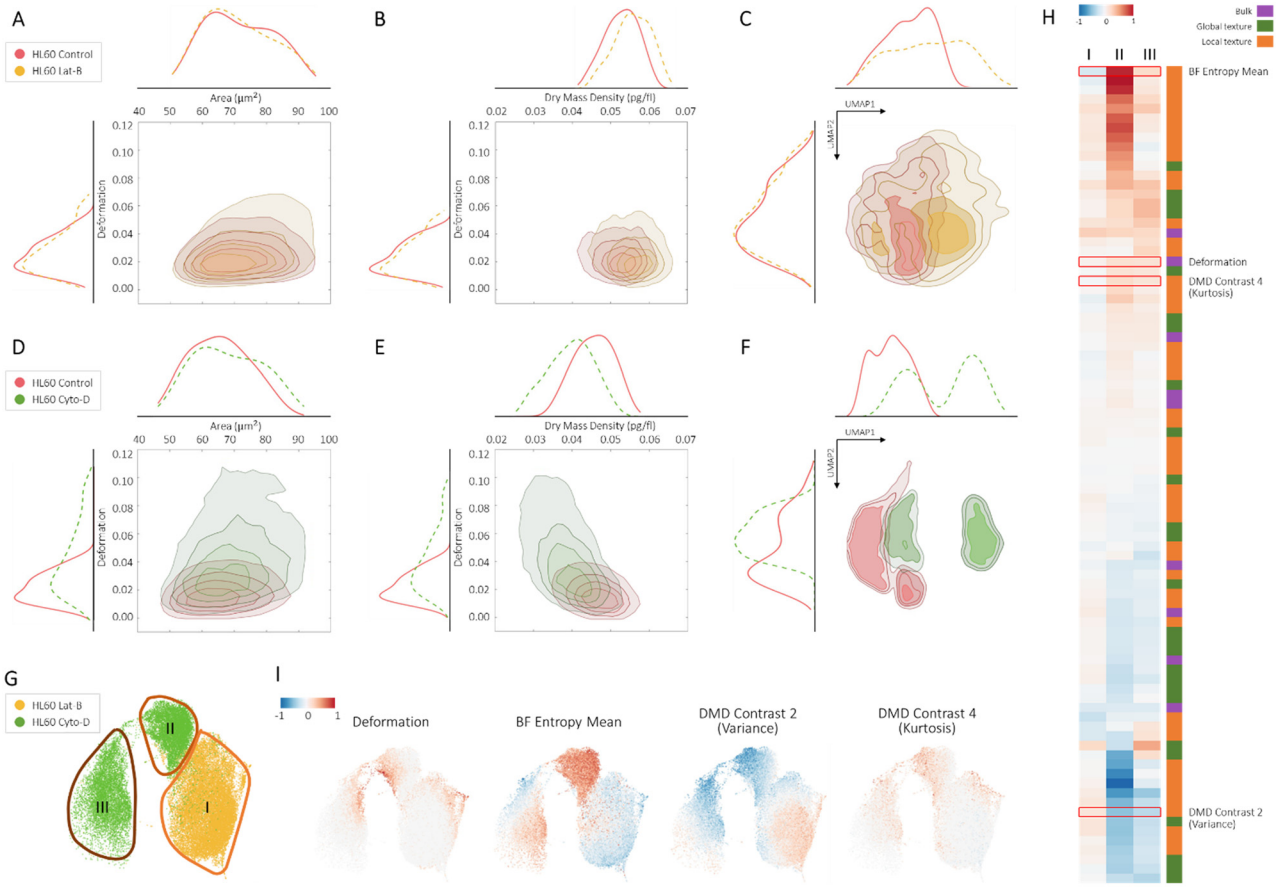

Fig. 4 Comparison of drug effects on human leukemia cells (HL60). (A and B) Lat-B treated cells (yellow) show an increased range of deformation and DMD over that of control cells (pink). (D and E) Cyto-D treated cells (green) show an increased range of deformation and a decreased range of DMD over that of control cells (pink). (C and F) Contour UMAP shows a clear trend and less overlap in the density of each control group *versus* the treated group. It means the effect of the drugs is clearly distinguishable through our QP-MORE system. (G) Lat-B treated cells (yellow) and Cyto-D treated cells (green) plotted on a scatter UMAP clearly show a distinction in their distribution over the entire 86 features extracted from the cell mask and the three complementary image contrasts. (H) Heatmap of all 86 features ranked and clustered in the order of greater meaned difference value, ranged between −1 (blue) to 1 (red). Mean difference is calculated per region as labeled in (G), where for each feature the treated cell values are subtracted by the mean of the control cells value of the corresponding feature, followed by averaging the value over the population. It shows different regions give unique 'fingerprint' of the features even within the same cell type treated with the same drug under the same condition (Fig. S5). (I) Four selected feature UMAPs showing the change of values for the respective feature in relation to the control over the whole population. Values are normalized to the range (−1, 1) for each feature. Red shows positive change, blue for negative change, and white represents no change.

unique biophysical outcomes: Lat-B preserves fragmented filaments but eliminates free monomers, whereas Cyto-D dismantles filaments into dispersed subunits. This mechanistic duality makes them an ideal testbed for QP-MORE's capacity to stratify nuanced biophysical/mechanical states.

Using QP-MORE, we observed that Cyto-D induced greater cell deformation than Lat-B (Fig. 4A and D), consistent with the previous study in which Cyto-D has led to more rapid filament disassembly.[53] Critically, treating HL60 cells with Cyto-D also resulted in a significant reduction in DMD (0.041 pg fl^{-1} *vs.* 0.036 pg fl^{-1} in controls; $d = -0.54$), while Lat-B caused a less significant change in DMD (Fig. 4B and E). We recognize the observed differences in DMD response between the two cell lines (Fig. 3B and 4B) and agree that investigating the underlying causes warrants further exploration. Potential factors include intrinsic variations in cytoskeletal architecture, actin dynamics, or cell-type-specific reactions to Lat-B. For example, HL60 cells, as suspension hematopoietic cells, exhibit a less developed cortical actin structure Fig. 4 Comparison of drug effects on human leukemia cells (HL60): (A, B) Lat-B treated cells (yellow) show an increased range of deformation and DMD over that of control cells (pink). (D, E) Cyto-D treated cells (green) show an increased range of deformation and a decreased range of DMD over that of control cells (pink). (C, F) Contour UMAP shows a clear trend and less overlap in the density of each control group *versus* the treated group. It means the effect of the drugs is clearly distinguishable through our QP-MORE system. (G) Lat-B treated cells (yellow) and Cyto-D treated cells (green) plotted on a scatter UMAP clearly show a distinction in their distribution over the entire 86 features extracted from the cell mask and the three complementary image contrasts. (H) Heatmap of all 86 features ranked and

clustered in the order of greater meaned difference value, ranged between −1 (blue) to 1 (red). Mean difference is calculated per region as labeled in (G), where for each feature the treated cell values are subtracted by the mean of the control cells value of the corresponding feature, followed by averaging the value over the population. It shows different regions give unique 'fingerprint' of the features even within the same cell type treated with the same drug under the same condition (Fig. S5). (I) Four selected feature UMAPs showing the change of values for the respective feature in relation to the control over the whole population. Values are normalized to the range (−1, 1) for each feature. Red shows positive change, blue for negative change, and white represents no change and rely more on dynamic actin remodeling for their function, whereas MDA-MB231 epithelial cells possess a more structured cytoskeleton with stress fibers that may respond differently to actin depolymerization.[54,55] Lat-B has been shown to induce variable morphological and mechanical responses across different cell types, including changes in volume, mass, and adhesion, depending on the baseline organization of the actin cytoskeleton.[56,57]

These findings highlight the critical role of cell context in interpreting biophysical responses to cytoskeletal perturbations and underscore the need for future mechanistic investigations.

Again, going beyond the bulk metrics, high-dimensional biophysical morphological analysis (*i.e.*, using all 86 features) reveal further heterogeneity in both drug treatment cases (Fig. 4C and F). When analysed together, the changes in the biophysical morphology in response to the two drugs can be clearly distinguished (see the clear segregation of the three populations in Fig. 4G). Furthermore, we also observe that the changes in the few subcellular textures, other than those discussed in the previous section, namely deformation, BF entropy mean, DMD contrast 2 (variance), and DMD contrast 4 (kurtosis), are more pronounced in the case of Cyto-D than that of Lat-B, *i.e.*, shows in denser red or blue. (Fig. 4H and I). Elevated BF entropy mean—BF means it is extracted from BF image—in Cyto-D treated cells reflects more disorder in (actin fragment) subcellular information against the control than that of Lat-B treated cells. The decrease in DMD contrast 2 (variance) in Cyto-D treated cells indicates that the DMD distribution is narrowed than the control cells, whereas the distribution has increased in the case of Lat-B treated cells (Fig. 4I). The clear contrast and trend in deformation and mass distribution metrics underscores QP-MORE's unique capacity to resolve mechanistic divergence invisible to bulk assays.

To quantify the advantage of subcellular-resolution biophysical profiling offered by QP-MORE, we compared it to the previous D–C method,[32] which is restricted to bulk metrics like deformability, optical opacity, and cell size. While D–C achieved moderate accuracy (78–94%) in classifying drug-treated cells in the two drug treatments, QP-

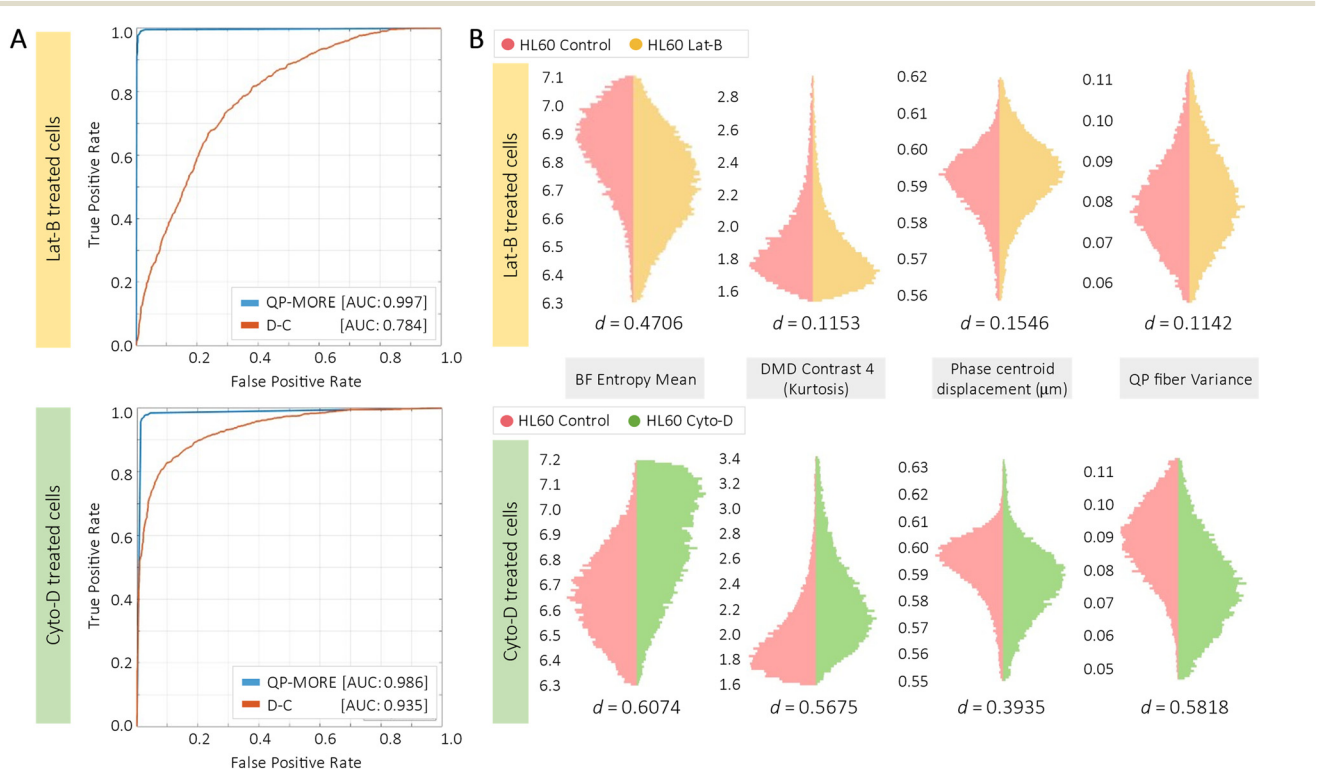

Fig. 5 QP-MORE performance compared to the D–C performance. (A) Receiver operating characteristic (ROC) curve comparing the performance of QP-MORE with D–C, (B) violin plots of four features: BF entropy mean, DMD contrast 4 (kurtosis), phase centroid displacement and QP fiber variance, analysed through MATLAB.

MORE further reached 99% accuracy (Fig. 5A)—a significant improvement attributable to its ability to resolve subcellular textural features, which are absent in conventional MORE.

QP-MORE could reveal the subtle differences in architectural biophysical changes in response to the two different drugs that bulk metrics overlook (Fig. 5B). Notably, we observe more significant changes in the subcellular texture randomness/asymmetry, *i.e.*, BF entropy mean, DMD contrast 4 (kurtosis), and mass density redistribution/shifts (*e.g.*, phase centroid displacement, QP fiber variance) in the case of Cyto-D-treated cells. QP-MORE thus expands biophysical cytometry from bulk phenotyping to architectural profiling, resolving drug-specific structural reorganizations critical for mechanistic studies.

Conclusions

QP-MORE represents a new advancement in biophysical cytometry, unifying quantitative phase imaging (QPI), bright-field textural analysis, and high-throughput deformability profiling into a single optofluidic platform without sacrificing the imaging throughput. By achieving subcellular resolution at >10 000 cells per s, QP-MORE overcomes the limitations of conventional deformability-based systems, which trade resolution for throughput or *vice versa*. This multimodal synergy enables new correlations between whole-cell mechanics (*e.g.*, deformability) and subcellular biophysical structures such as mass density and its distributions—all tested by our calibrated morpho-rheological instrumentation and backend analysis.

In dissecting drug responses in leukemia and breast cancer cell types, QP-MORE not only resolved drug-specific subcellular signatures (*i.e.*, latrunculin B *vs.* cytochalasin D) but also achieved 99% accuracy—surpassing D–C (78–94%), classified by a neural network model (10-fold cross-validation) with 10% test sample. Note that the classification is done on the same sample datasets to compare the results interpretation accuracy when having 86 features against 6 features. This advancement could substantiate the significance of biophysical cytometry in supporting frontier research in cancer biology (*e.g.*, detecting pre-metastatic circulating tumor cells), immunology (*e.g.*, profiling immune cell mechano-activation), and drug discovery (*e.g.*, mechanophenotypic compound screens).

To realize QP-MORE's full potential, three further synergistic advancements are critical: (1) molecular specificity: integrating ultrafast fluorescence imaging[4,11,58] could enable simultaneous readouts of biomolecular data (surface markers, organelle-specific tags) together with biophysical phenotypes, empowering truly molecularly-specific mechanobiology. (2) Size-insensitive single-cell imaging robustness: better alignment and focusing of the single-cell stream of a heterogeneous sample—with sizes ranging from a few microns to tens of microns—in ultrafast microfluidic system is essential to ensure high-quality imaging and thus subcellular biophysical morphological profiling. Recent advances in particle manipulation could be implemented with QP-MORE, *e.g.*, dispersion-free inertial focusing (DIF),[59] which demonstrated uniform cell positioning with >95% imaging yield. (3) Biophysics-to-omics pipelines: coupling QP-MORE with microfluidic cell sorting could isolate targeted cells with specific mechanical/biophysical phenotypes of interest (*e.g.*, drug-resistant cells) for downstream molecular analysis (*e.g.*, single-cell RNA-seq), directly linking subcellular architecture to transcriptional programs.

We note a minor batch effect across experiments, mainly due to unavoidable variations in imaging system configurations (*e.g.*, laser power fluctuations, photodetector noise). Nevertheless, our QP-MORE analyses of drug treatments are reproducible at the population level (see Fig. S6). In addition, computational batch correction methods, including deep learning-based approaches,[60] may be applied to QP-MORE data to support robust downstream morphological analyses, particularly when integrating data from different dates or systems.

The fusion of high-throughput biophysics and omics could democratize biophysical cytometry, enabling cost-effective, label-free cell sorting for liquid biopsies or immunotherapy monitoring. Early work in image-activated sorting already demonstrates this potential,[58,61,62] suggesting a future where cells are stratified by biomechanical states rather than fluorescent labels. We note that realizing real-time QP-MORE-based sorting will require substantial advances in analysis speed, as current offline processing is too slow for practical sorting applications. Recent progress in hardware acceleration—particularly with FPGAs optimized for deep learning inference—has enabled classification latencies as low as tens of microseconds per cell at high throughput, making real-time, image-based biophysical sorting increasingly feasible.[63–65] Overcoming the trade-off between computational speed and classification accuracy will be critical for future clinical translation.

Deployed in clinics, QP-MORE could further redefine cost-effective diagnostics—detecting malignancy or immune dysfunction in blood—while accelerating drug development by connecting mechanophenotypes to molecular targets. QP-MORE could spearhead a new foundation for practical biophysical cytometry where cellular biophysics informs precision therapeutics and transforms our understanding of disease.

Methods

Sample preparation

Cell culture. HL60 (American Type Culture Collection, ATCC) cell culture medium consisted of 90% Roswell Park Memorial Institute (RPMI)-1640 medium (Thermo Fisher Scientific), 10% fetal bovine serum (FBS), and 1% 100× antibiotic–antimycotic (Thermo Fisher Scientific). MDA-MB231 cells (ATCC) were cultured in a medium consisting of Dulbecco's modified Eagle medium (DMEM) (Gibco), 10%

PBS, and 1% 100× antibiotic–antimycotic (Thermo Fisher Scientific). The cells were placed in a CO_2 incubator at 37 °C with 5% CO_2. The cell culture media was replaced twice a week based on cell confluence. Antibiotic–antimycotic was used to prevent bacterial and fungal contamination. Throughout cell cultivation, a light microscope was used to assess cell morphologies on a regular basis.

Cell harvest. HL60 cells were developed in suspension, so trypsinisation is not necessary. The medium containing the cells was centrifuged at 1000 rpm for 5 min, and the supernatant was discarded. The pellet was resuspended in 3 mL of warmed medium. For adherent cells like MDA-MB231, trypsinisation was needed to harvest the cells. Firstly, the medium in the culture flask was discarded, and then the surface was rinsed with 3 mL of 1× PBS to remove the leftover FBS. Following that, 3 mL of 0.25% trypsin–EDTA (Gibco) was added to the culture flask and placed in an incubator at 37 °C for 5 min. To stop the trypsinisation, 4 mL of cell culture medium was added, and the mixture was centrifuged at 1000 rpm for 5 min. The supernatant was removed, and the cell samples were ready for use after resuspending the pellet with 3 mL of warm medium.

Drug treatments

Cyto-D (Sigma-Aldrich, catalogue no. C8273) and Lat-B (Sigma-Aldrich, catalogue no. L5288) were purchased in powder form and required dissolving before usage. To prepare a 10 μM Cyto-D stock solution, the powdered drugs were sonicated to dissolve in 1× PBS and incubated at 37 °C for 10 min. The stock solution was split into 1 mL aliquots and kept at −20 °C for later use. Lat-B stock solution (100 ng mL^{-1}) was prepared with 1 mg Lat-B powder dissolved in 1 mL 1% v/v dimethyl sulfoxide (DMSO, Sigma Aldrich) and diluted 10 000× with 1× PBS. It was then incubated at 37 °C for 30 min.

HL60 and MDA-MB231 cells were seeded in a 6-well plate at a density of 10^5 per well. Each drug was added to the prepared sample with the desired concentration, and 1% v/v DMSO in 1x PBS was added to the control sample. The samples were then kept at 37 °C for 24 h before being harvested for imaging. The subsequent deformability measurements were conducted at room temperature (25 °C). For more detailed drug treatment processes, refer to the drug protocols.

Microfluidic chip fabrication

Wafer patterning by photolithography. Firstly, a layer of photoresist (SU-8 3025, MicroChem) was coated on a silicon wafer using a spin coater (spinNXG-P1, Apex Instruments) to reach an even layer of approximately 20 μm. The coated silicon wafer was then soft-baked twice (at 65 °C for 3 min and 95 °C for 10 min). The cooled-down silicon water was placed onto a soft lithography machine (SF-100 XCEL, Intelligent Micro Patterning), and the channel pattern designed by computer-aided design (CAD) was loaded onto the machine. After photolithography of a 6.5 second exposure time, the wafer was placed on a hot plate (at 65 °C for 1 min and 95 °C for 5 min) for post-exposure bake. After it cooled down to room temperature, it was submerged in SU-8 developer (MicroChem) for 5 min for photoresist development. Finally, it was rinsed using isopropyl alcohol and dried using pressurised air. The patterned silicon wafer was then placed on a 150 °C hot plate for 20 min to cross-link the material to strengthen the patterned wafer.

Moulding by soft lithography. A mixture of PDMS with the curing agent—of a mixing ratio of 9 : 1 to achieve higher stiffness, rather than the normal practice of 10 : 1—was used as the material for the microfluidic channel (SYLGARD 184 silicone elastomer, Dow Corning). After pouring the mixture onto the patterned silicon wafer, a specially designed acrylic block was placed near the imaging region to control the thickness (into ~1 mm) of the PDMS layer for ideal imaging quality. The channel was then cured on a hot plate at 150 °C for 1 h. After demoulding the channel from the wafer, inlet and outlet holes were punched using a biopsy punch (Miltex 33-31 AA, Integra LifeSciences) for plastic tubing insertion. The PDMS mould and a 25 mm × 50 mm cover glass were then treated with an oxygen plasma machine (PDC-002, Harrick Plasma) for surface bonding activation. After sticking the two treated surfaces, the chip was placed on an 80 °C hot plate for 2 h to strengthen the bond. An overview of the microfluidic chip fabrication can be found in Fig. S8.

Microfluidic design considerations

The microfluidic chip design was adopted and modified from the original design for the previous deformability cytometry work[32] (Fig. S2). To fit the objective lens of multi-ATOM to the imaging region of the chip, the length of the channel was increased. The length of the narrow part of the channel after the sudden constriction was kept at 300 μm. Before the constriction of channel width, the wider section was made longer to provide a wider region for imaging undeformed cells. Circular pillars near the inlet of the chip—with a separation of 20 μm—were added as filters to prevent any debris larger than 20 μm from reaching and clogging the constriction channel. The centre square constriction channel has a cross-section of 20 μm × 20 μm—it can be modified to fit the size of the cells for different cell types. For better-quality imaging, the sample size should be between 50% and 90% of the channel size to ensure a large enough shear gradient to induce deformation as well as to prevent the cells from touching the channel walls.

Imaging system setup

Loading microfluidic chip. A deformation-inducing microfluidic chip was initialised by filling up with PBS, and it was ensured that there were no air bubbles remaining within the channel to eliminate any flow bias due to the bubbles. A 20 μm × 20 μm constriction channel was used for imaging PAAm beads, HL60 cells and MDA-MB231 cells. The

concentration of cell samples was prepared to approximately 2×10^5 cells per mL. 10 μm polystyrene beads were then added to the cell sample for flow rate calibration at intervals. The mixture was then filtered using a 20 μm cell strainer (pluriStrainer® 20 μm, pluriSelect Life Science) to control the cell size for better focusing and hence deformation analysis. Filtering is critical as this prevents any particle that is larger than the constriction channel width from causing clogging. The filtered sample was then added to a 10 mL syringe (SS + 10 L, Terumo) with a syringe needle (25 G × 5/8″, Terumo) attached to it. After connecting the syringe with the microfluidic chip *via* the plastic tubing (BB31695-PE/2, Scientific Commodities, Inc.), the syringe was loaded onto a hydraulic pump (LSP01, Longerpump), and the desired flow rate was set. The ratio of the flow rate of the sample to the sheath was kept at 1 : 3 for the best performance.

Data analysis

Features extraction. Biophysical parameters were extracted (Fig. 1C) using custom MATLAB codes from the different modes of reconstructed cell images (Fig. 1B). A binary mask was first delineated and used to eliminate the background of cell images to only consider the region of interest. The nature of features extracted can be categorised into three groups: (1) bulk parameters from mask, (2) global textural parameters from both optical and mass density, and (3) local textural parameters from both optical and mass density. Features extracted from optical density are obtained from the bright-field (BF) images, while mass density features are extracted from DMD map obtained from QPI images[66] (Fig. 4H, S5 and Table S1). The quantification of 86 extracted features from each imaged cell creates the fingerprint of each cell. For more details, please refer to our previous work.[34]

Machine learning-based classification. To compare the classification accuracy of QP-MORE (using 86 morphological features) and D–C (using 6 deformability features), we performed neural network classification (NNC) (MATLAB Classification Learner). For both feature sets extracted from each drug-treated sample as depicted in Fig. 3 and 4, respectively, we used a narrow neural network model, which consists of a single fully connected hidden layer with 10 neurons and ReLU activation. Models were trained for up to 1000 iterations, with standardized inputs and no regularization ($\lambda = 0$). Misclassification costs and optimizer settings were kept at their default values. To reduce overfitting and improve generalizability, we used 10-fold cross-validation throughout. This approach resulted in a validation accuracy of 99.1% for QP-MORE and 75.1% for D–C in Lat-B treated HL60 cells. For Cyto-D treated HL60 cells, QP-MORE achieved a validation accuracy of 97.5%, while D–C yielded 86%. A test sample comprising 10% of the data was then used to evaluate the test accuracy, with the results presented in Fig. 5A and the complementary confusion matrix in Fig. S7.

Data visualization. Using the 86 extracted features of each cell, scatter UMAP was created (*i.e.*, dimension reduction from 86-D to 2-D) over the whole cell population. The raw population includes an unwanted population, so gating was done on the UMAP to gate out the debris or the cell aggregates. With the gated cells of interest, UMAP was created to follow the overall trend of the whole cell population. UMAP was also created for each feature, over the gated population of each sample and the gated population of control and treated cells put together—to see the trend between the control and the treated population. It was then followed by multiple different graphical plots, including the violin plot, contour UMAP with region analysis, and the projected density plot to analyze the results from varying perspectives. These multiple types of plots were used to quantitatively compare and distinguish the trend and the drug effect for different sample conditions. Later stages of data analysis also include a selection of more significant features—20 features with a higher Cliff's delta value—which were used to construct a heatmap that shows and distinguishes the trend between each set of data (Fig. 3E).

Author contributions

J. G., and K. K. T. conceptualized and supervised the study. E. H. Y. C. performed the QP-MORE imaging experiments. T. L. and E. H. Y. C. performed the image analysis. E. H. Y. C., K. K., F. R., M. K., and M. K. designed the microfluidic experiments of QP-MORE. T. L., E. H. Y. C., J. G., and K. K. T. wrote the manuscript with all other authors' inputs and comments.

Conflicts of interest

There are no conflicts to declare.

Data availability

Supplementary information is available. See DOI: **https://doi.org/10.1039/D5LC00381D**.

The dataset used in this paper can be accessed from the following link for your reference: **https://doi.org/10.5281/zenodo.15097963**. Due to the large size of the raw data files, only relevant analysed files were uploaded. The complete data supporting the findings of this study are available from the corresponding author upon reasonable request.

Code availability: Customized MATLAB code relevant to this paper can be accessed on the following link for your reference: **https://doi.org/10.5281/zenodo.15097963**.

Acknowledgements

Sam Ho cultured and treated the cell samples with drugs. The work is supported by Advanced Biomedical Instrumentation Center, the Research Grants Council (grant no. 17125121, 14125924, RFS2021-7S06, R7003-21) and the Innovation and Technology Commission of the Hong Kong Special

Administrative Region of China (grant no. ITS/318/22FP, ITS/408/23FP), Platform Technology Funding of the University of Hong Kong.

References

1 D. M. D. Siu, K. C. M. Lee, B. M. F. Chung, J. S. J. Wong, G. Zheng and K. K. Tsia, *Lab Chip*, 2023, **23**, 1011–1033.
2 C. Gao, T. Zhang, Y. Wei, Q. Liu, L. Ma, M. Gao, X. Zhao, Y. Wang, D. Chen, L. Sun, J. Wang and J. Chen, *ACS Sens.*, 2023, **8**, 3498–3509.
3 Y. Han, Y. Gu, A. C. Zhang and Y. H. Lo, *Lab Chip*, 2016, **16**, 4639–4647.
4 N. S. Barteneva, E. Fasler-Kan and I. A. Vorobjev, *J. Histochem. Cytochem.*, 2012, **60**, 723–733.
5 L. Samsel, P. K. Dagur, N. Raghavachari, C. Seamon, G. J. Kato and J. P. McCoy Jr, *Cytometry, Part B*, 2013, **84**, 379–389.
6 A. S. Rane, J. Rutkauskaite, A. deMello and S. Stavrakis, *Chem*, 2017, **3**, 588–602.
7 S. P. Perfetto, P. K. Chattopadhyay and M. Roederer, *Nat. Rev. Immunol.*, 2004, **4**, 648–655.
8 Y. Han, Y. Gu, A. C. Zhang and Y.-H. Lo, *Lab Chip*, 2016, **16**, 4639–4647.
9 P. Rosendahl, K. Plak, A. Jacobi, M. Kraeter, N. Toepfner, O. Otto, C. Herold, M. Winzi, M. Herbig, Y. Ge, S. Girardo, K. Wagner, B. Baum and J. Guck, *Nat. Methods*, 2018, **15**, 355–358.
10 H. Kanno, K. Hiramatsu, H. Mikami, A. Nakayashiki, S. Yamashita, A. Nagai, K. Okabe, F. Li, F. Yin, K. Tominaga, O. F. Bicer, R. Noma, B. Kiani, O. Efa, M. Büscher, T. Wazawa, M. Sonoshita, H. Shintaku, T. Nagai, S. Braun, J. P. Houston, S. Rashad, K. Niizuma and K. Goda, *Nat. Commun.*, 2024, **15**, 7376.
11 H. Mikami, M. Kawaguchi, C.-J. Huang, H. Matsumura, T. Sugimura, K. Huang, C. Lei, S. Ueno, T. Miura, T. Ito, K. Nagasawa, T. Maeno, H. Watarai, M. Yamagishi, S. Uemura, S. Ohnuki, Y. Ohya, H. Kurokawa, S. Matsusaka, C.-W. Sun, Y. Ozeki and K. Goda, *Nat. Commun.*, 2020, **11**, 1162.
12 N. T. Shaked, S. A. Boppart, L. V. Wang and J. Popp, *Nat. Photonics*, 2023, **17**, 1031–1041.
13 D. L. Pham, A. A. Gillette, J. Riendeau, K. Wiech, E. C. Guzman, R. Datta and M. C. Skala, *J. Biomed. Opt.*, 2025, **29**, S22702.
14 T. Blasi, H. Hennig, H. D. Summers, F. J. Theis, J. Cerveira, J. O. Patterson, D. Davies, A. Filby, A. E. Carpenter and P. Rees, *Nat. Commun.*, 2016, **7**, 10256.
15 T. P. Miettinen and M. Björklund, *Cell Rep.*, 2015, **13**, 2610–2620.
16 M. Guo and B. A. Hay, *Curr. Opin. Cell Biol.*, 1999, **11**, 745–752.
17 W. Xu, R. Mezencev, B. Kim, L. Wang, J. McDonald and T. Sulchek, *PLoS One*, 2012, **7**, e46609.
18 L. R. Smith, S. Cho and D. E. Discher, *Physiology*, 2018, **33**, 16–25.
19 Z. Su, Z. Chen, K. Ma, H. Chen and J. W. K. Ho, *Biophys. Rev.*, 2022, **14**, 1197–1209.
20 S. Yadav, M. J. Barton and N.-T. Nguyen, *J. Biomech.*, 2019, **86**, 1–7.
21 F. A. Pennacchio, P. Nastały, A. Poli and P. Maiuri, *Front. Bioeng. Biotechnol.*, 2020, **8**, 596746.
22 C. Uhler and G. V. Shivashankar, *Trends Cancer*, 2018, **4**, 320–331.
23 J. Zhang, F. Alisafaei, M. Nikolić, X. A. Nou, H. Kim, V. B. Shenoy and G. Scarcelli, *Small*, 2020, **16**, e1907688.
24 D. Di Carlo, *SLAS Technol.*, 2012, **17**, 32–42.
25 K. C. M. Lee, J. Guck, K. Goda and K. K. Tsia, *Trends Biotechnol.*, 2021, **39**, 1249–1262.
26 Q. Rezard, G. Perret, J. C. Gerbedoen, D. Pekin, F. Cleri, D. Collard, C. Lagadec and M. C. Tarhan, Developing A Mems Device for High-Throughput Multi-Parameter Single Cell Biophysical Analysis, *2021 IEEE 34th International Conference on Micro Electro Mechanical Systems (MEMS)*, 2021, pp. 494–497, **https://ieeexplore.ieee.org/document/9375176?signout=success**.
27 D. R. Gossett, H. T. K. Tse, S. A. Lee, Y. Ying, A. G. Lindgren, O. O. Yang, J. Rao, A. T. Clark and D. Di Carlo, *Proc. Natl. Acad. Sci. U. S. A.*, 2012, **109**, 7630–7635.
28 M. Chapman, V. Rajagopal, A. Stewart and D. J. Collins, *Lab Chip*, 2024, **24**, 3036–3063.
29 Y. Chen, C. Ni, L. Jiang, Z. Ni and N. Xiang, *Small*, 2024, **20**, e2303962.
30 M. Urbanska, H. E. Muñoz, J. Shaw Bagnall, O. Otto, S. R. Manalis, D. Di Carlo and J. Guck, *Nat. Methods*, 2020, **17**, 587–593.
31 N. Toepfner, C. Herold, O. Otto, P. Rosendahl, A. Jacobi, M. Kräter, J. Stächele, L. Menschner, M. Herbig, L. Ciuffreda, L. Ranford-Cartwright, M. Grzybek, Ü. Coskun, E. Reithuber, G. Garriss, P. Mellroth, B. Henriques-Normark, N. Tregay, M. Suttorp, M. Bornhäuser, E. R. Chilvers, R. Berner and J. Guck, *eLife*, 2018, **7**, e29213.
32 O. Otto, P. Rosendahl, A. Mietke, S. Golfier, C. Herold, D. Klaue, S. Girardo, S. Pagliara, A. Ekpenyong, A. Jacobi, M. Wobus, N. Töpfner, U. F. Keyser, J. Mansfeld, E. Fischer-Friedrich and J. Guck, *Nat. Methods*, 2015, **12**, 199–202.
33 M. Xavier, P. Rosendahl, M. Herbig, M. Kräter, D. Spencer, M. Bornhäuser, R. O. C. Oreffo, H. Morgan, J. Guck and O. Otto, *Integr. Biol.*, 2016, **8**, 616–623.
34 D. M. D. Siu, K. C. M. Lee, M. C. K. Lo, S. V. Stassen, M. Wang, I. Z. Q. Zhang, H. K. H. So, G. C. F. Chan, K. S. E. Cheah, K. K. Y. Wong, M. K. Y. Hsin, J. C. M. Ho and K. K. Tsia, *Lab Chip*, 2020, **20**, 3696–3708.
35 S. Golfier, P. Rosendahl, A. Mietke, M. Herbig, J. Guck and O. Otto, *Cytoskeleton*, 2017, **74**, 283–296.
36 M. Urbanska, P. Rosendahl, M. Kräter and J. Guck, *Methods Cell Biol.*, 2018, **147**, 175–198.
37 Y. Park, C. Depeursinge and G. Popescu, *Nat. Photonics*, 2018, **12**, 578–589.
38 K. C. M. Lee, M. Wang, K. S. E. Cheah, G. C. F. Chan, H. K. H. So, K. K. Y. Wong and K. K. Tsia, *Cytometry, Part A*, 2019, **95**, 510–520.
39 K. C. M. Lee, A. K. S. Lau, A. H. L. Tang, M. Wang, A. T. Y. Mok, B. M. F. Chung, W. Yan, H. C. Shum, K. S. E. Cheah,

G. C. F. Chan, H. K. H. So, K. K. Y. Wong and K. K. Tsia, *J. Biophotonics*, 2019, **12**, e201800479.
40 A. K. S. Lau, H. C. Shum, K. K. Y. Wong and K. K. Tsia, *Lab Chip*, 2016, **16**, 1743–1756.
41 T. T. W. Wong, A. K. S. Lau, K. K. Y. Ho, M. Y. H. Tang, J. D. F. Robles, X. Wei, A. C. S. Chan, A. H. L. Tang, E. Y. Lam, K. K. Y. Wong, G. C. F. Chan, H. C. Shum and K. K. Tsia, *Sci. Rep.*, 2014, **4**, 3656.
42 M. C. K. Lo, D. M. D. Siu, K. C. M. Lee, J. S. J. Wong, M. C. F. Yeung, M. K. Y. Hsin, J. C. M. Ho and K. K. Tsia, *Adv. Sci.*, 2024, **11**, 2307591.
43 Z. Zhang, K. C. M. Lee, D. M. D. Siu, M. C. K. Lo, Q. T. K. Lai, E. Y. Lam and K. K. Tsia, *Commun. Biol.*, 2023, **6**, 449.
44 D. Pirone, J. Lim, F. Merola, L. Miccio, M. Mugnano, V. Bianco, F. Cimmino, F. Visconte, A. Montella, M. Capasso, A. Iolascon, P. Memmolo, D. Psaltis and P. Ferraro, *Nat. Photonics*, 2022, **16**, 851–859.
45 E. R. Polanco, T. E. Moustafa, A. Butterfield, S. D. Scherer, E. Cortes-Sanchez, T. Bodily, B. T. Spike, B. E. Welm, P. S. Bernard and T. A. Zangle, *Commun. Biol.*, 2022, **5**, 794.
46 C. F. Otesteanu, M. Ugrinic, G. Holzner, Y.-T. Chang, C. Fassnacht, E. Guenova, S. Stavrakis, A. deMello and M. Claassen, *Cells Rep. Methods*, 2021, **1**(6), 100094.
47 L. Tian and L. Waller, *Opt. Express*, 2015, **23**, 11394–11403.
48 Q. Xiao, Y. He, M. H. Rahman, G. Cheng, R. Zhou and Y.-P. Ho, *View*, 2023, **4**, 20220049.
49 A. Mietke, O. Otto, S. Girardo, P. Rosendahl, A. Taubenberger, S. Golfier, E. Ulbricht, S. Aland, J. Guck and E. Fischer-Friedrich, *Biophys. J.*, 2015, **109**, 2023–2036.
50 D. Di Carlo, *Lab Chip*, 2009, **9**, 3038–3046.
51 H. Kanno, H. Mikami and K. Goda, *Opt. Lett.*, 2020, **45**, 2339–2342.
52 I. Spector, N. R. Shochet, D. Blasberger and Y. Kashman, *Cell Motil. Cytoskeleton*, 1989, **13**, 127–144.
53 T. Wakatsuki, B. Schwab, N. C. Thompson and E. L. Elson, *J. Cell Sci.*, 2001, **114**, 1025–1036.
54 S. H. Zigmond, *J. Cell Biol.*, 1978, **77**, 269–287.
55 L. Cassimeris, H. McNeill and S. H. Zigmond, *J. Cell Biol.*, 1990, **110**, 1067–1075.
56 I. Spector, N. R. Shochet, Y. Kashman and A. Groweiss, *Science*, 1983, **219**, 493–495.
57 J. Stricker, T. Falzone and M. L. Gardel, *J. Biomech.*, 2010, **43**, 9–14.
58 D. Schraivogel, T. M. Kuhn, B. Rauscher, M. Rodríguez-Martínez, M. Paulsen, K. Owsley, A. Middlebrook, C. Tischer, B. Ramasz, D. Ordoñez-Rueda, M. Dees, S. Cuylen-Haering, E. Diebold and L. M. Steinmetz, *Science*, 2022, **375**, 315–320.
59 K. C. M. Lee, B. M. F. Chung, D. M. D. Siu, S. C. K. Ho, D. K. H. Ng and K. K. Tsia, *Lab Chip*, 2024, **24**, 4182–4197.
60 X. Wei, A. K. Lau, Y. Xu, K. K. Tsia and K. K. Wong, *Biomed. Opt. Express*, 2015, **6**, 3855–3864.
61 N. Nitta, T. Sugimura, A. Isozaki, H. Mikami, K. Hiraki, S. Sakuma, T. Iino, F. Arai, T. Endo, Y. Fujiwaki, H. Fukuzawa, M. Hase, T. Hayakawa, K. Hiramatsu, Y. Hoshino, M. Inaba, T. Ito, H. Karakawa, Y. Kasai, K. Koizumi, S. Lee, C. Lei, M. Li, T. Maeno, S. Matsusaka, D. Murakami, A. Nakagawa, Y. Oguchi, M. Oikawa, T. Ota, K. Shiba, H. Shintaku, Y. Shirasaki, K. Suga, Y. Suzuki, N. Suzuki, Y. Tanaka, H. Tezuka, C. Toyokawa, Y. Yalikun, M. Yamada, M. Yamagishi, T. Yamano, A. Yasumoto, Y. Yatomi, M. Yazawa, D. Di Carlo, Y. Hosokawa, S. Uemura, Y. Ozeki and K. Goda, *Cell*, 2018, **175**, 266–276.e213.
62 N. Nitta, T. Iino, A. Isozaki, M. Yamagishi, Y. Kitahama, S. Sakuma, Y. Suzuki, H. Tezuka, M. Oikawa, F. Arai, T. Asai, D. Deng, H. Fukuzawa, M. Hase, T. Hasunuma, T. Hayakawa, K. Hiraki, K. Hiramatsu, Y. Hoshino, M. Inaba, Y. Inoue, T. Ito, M. Kajikawa, H. Karakawa, Y. Kasai, Y. Kato, H. Kobayashi, C. Lei, S. Matsusaka, H. Mikami, A. Nakagawa, K. Numata, T. Ota, T. Sekiya, K. Shiba, Y. Shirasaki, N. Suzuki, S. Tanaka, S. Ueno, H. Watarai, T. Yamano, M. Yazawa, Y. Yonamine, D. Di Carlo, Y. Hosokawa, S. Uemura, T. Sugimura, Y. Ozeki and K. Goda, *Nat. Commun.*, 2020, **11**, 3452.
63 A. Isozaki, H. Mikami, H. Tezuka, H. Matsumura, K. Huang, M. Akamine, K. Hiramatsu, T. Iino, T. Ito, H. Karakawa, Y. Kasai, Y. Li, Y. Nakagawa, S. Ohnuki, T. Ota, Y. Qian, S. Sakuma, T. Sekiya, Y. Shirasaki, N. Suzuki, E. Tayyabi, T. Wakamiya, M. Xu, M. Yamagishi, H. Yan, Q. Yu, S. Yan, D. Yuan, W. Zhang, Y. Zhao, F. Arai, R. E. Campbell, C. Danelon, D. Di Carlo, K. Hiraki, Y. Hoshino, Y. Hosokawa, M. Inaba, A. Nakagawa, Y. Ohya, M. Oikawa, S. Uemura, Y. Ozeki, T. Sugimura, N. Nitta and K. Goda, *Lab Chip*, 2020, **20**, 2263–2273.
64 M. Wang, K. C. M. Lee, B. M. F. Chung, S. V. Bogaraju, H. C. Ng, J. S. J. Wong, H. C. Shum, K. K. Tsia and H. K. H. So, *IEEE Trans. Neural Netw. Learn. Syst.*, 2022, **33**, 2853–2866.
65 T. Ding, K. C. M. Lee, K. K. Tsia, T. N. Siegel, D. Di Carlo and K. Goda, *Nat. Rev. Bioeng.*, 2025, DOI: **10.1038/s44222-025-00334-1**.
66 H. Zhao, P. H. Brown and P. Schuck, *Biophys. J.*, 2011, **100**, 2309–2317.